ACS Photonics

pubs.acs.org/journal/apchd5

Article

Active Metasurface Thermal Emitters by Metallic Polymers

Ting-Hsuan Chen,[†] Qizhang Li,[†] Xubing Wu,[†] Kyle Hulle, Pei-Jan Hung, Qingsong Fan, Ching-Tai Fu, and Po-Chun Hsu*

Cite This: *ACS Photonics* 2026, 13, 2338−2347

Read Online

ACCESS | Metrics & More | Article Recommendations | Supporting Information

ABSTRACT: Conducting polymers (CPs) have been versatile and effective materials for dynamically controlling optical properties with applications ranging from electrochromic windows and displays to variable infrared (IR) emittance devices and terahertz modulators. In particular, its biocompatibility, flexibility, reversibility, solution processability, and nonvolatile switching make it suitable for radiative thermoregulation under various application scenarios. However, the tunability of most CP-based variable thermal emittance devices is limited by the transmission-tuning mechanism of CPs and their thin-film configuration. Here, we numerically and experimentally demonstrate that intrinsically reflective CPs and properly designed metasurface structures can improve the performance. The IR emissivity tunability is achieved by synthesizing solution-processable polyaniline doped with camphor sulfonic acid (PANI-CSA) and characterizing the complex refractive indices at its conducting and insulating state. A forward-designed broadband wide-angle metasurface emitter based on an asymmetric Fabry−Pérot cavity and gap surface plasmon resonance effectively utilizes the lossy dielectric properties at its insulating state for the high-emissivity mode. When the conducting state is switched, the metasurface becomes highly metallic and reflective, resulting in the low-emissivity mode. This study marks a new approach as we perform the co-design of macromolecular and photonic structure to enable solution-processable active metasurfaces.

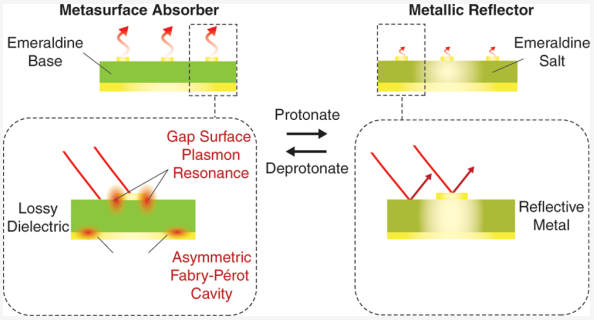

KEYWORDS: *tunable thermal emitter, active metasurface, polyaniline, gap surface plasmon, asymmetric Fabry−Pérot, solution processable, molecular and photonic co-design*

SIGNIFICANCE STATEMENT

This cross-disciplinary work demonstrates the material design principle to achieve the conjugated polymer-based variable thermal emitter with maximal emissivity contrast both spectrally and angularly, thanks to the codevelopment of bottom-up polymer synthesis, infrared optical conductivity characterization, and metasurface engineering. It numerically and experimentally achieved near-unity emissivity by the moderately doped conjugated polymer metasurface, with the ability to switch to very low emissivity by doping the polymer to a highly metallic state, which has been unobtainable by the conventional off-the-shelf or electropolymerized polymers with a loss-dominated optical property. The vast degrees of freedom, strong light−matter interactions, and ultrathin thickness enabled by optical metasurface theories provide unprecedented advantages.

INTRODUCTION

Incorporating actively tunable materials with metasurfaces allows the modulation of electromagnetic waves for applications including beam steering,[1,2] holography,[3] thermoregulation,[4−6] directional emission,[7,8] and color display.[9−13] The optical properties of tunable materials can be controlled through various mechanisms, such as phase transformation,[14,15] redox reaction,[16,17] charge carrier dynamics,[18−22] and defect engineering.[23,24] For example, thermochromic materials offer the benefit of undergoing a complete metal-to-insulator transition (MIT) in response to the temperature. The significant contrast from transmissive to reflective also provides a large tuning space between the two states.[25] Many inorganic phase-changing materials offer significant potential but are often influenced by their transition temperature and stability.[26] These challenges could be addressed through strategies such as precise stoichiometric control and advanced fabrication processes, which allow for better control over transformations and defects.[27]

Received: September 1, 2025
Revised: March 25, 2026
Accepted: March 26, 2026
Published: April 7, 2026

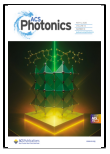

https://doi.org/10.1021/acsphotonics.5c02077
ACS Photonics 2026, 13, 2338−2347

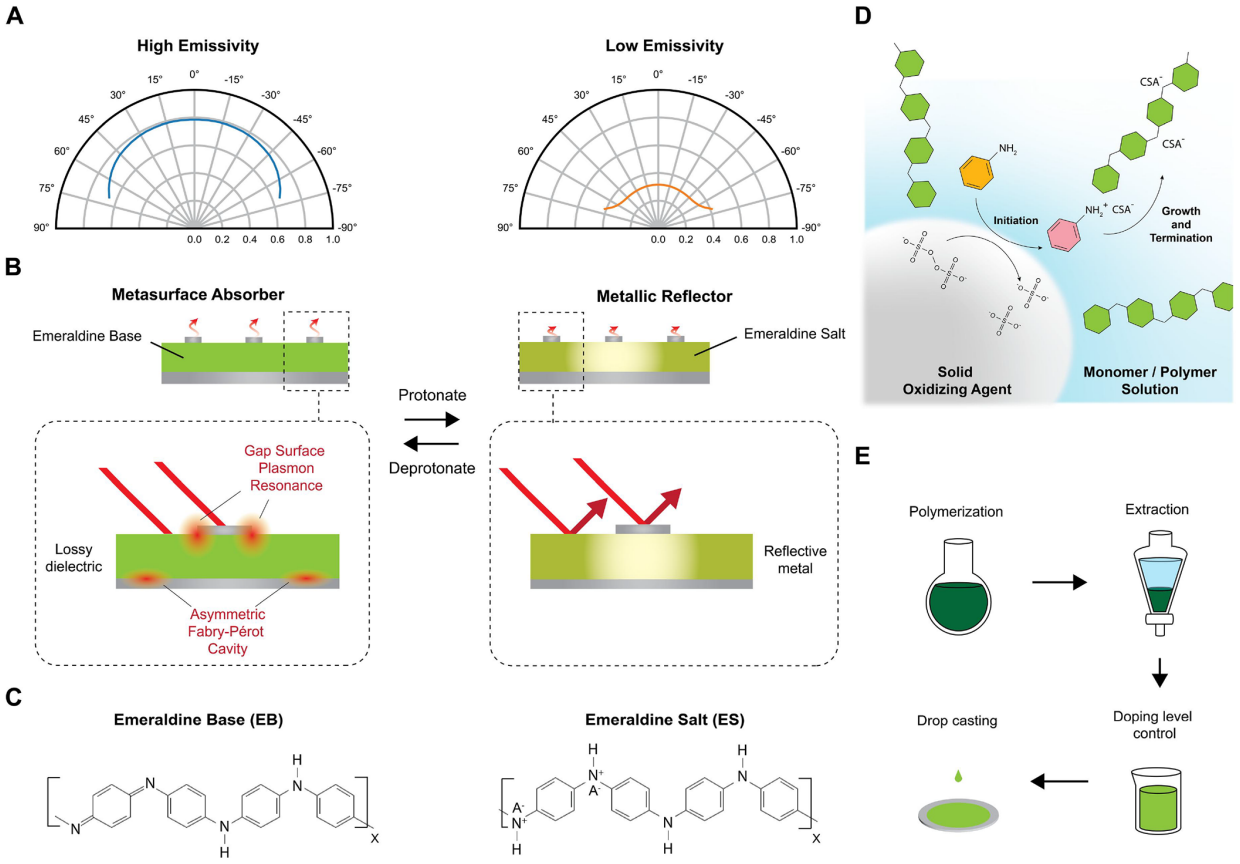

Figure 1. Solution-processable CP in a dynamically tunable metasurface. (A) Working principle. The metasurface is tunable between high and low emissivity by modulating the active material spacer between a lossy dielectric and a reflective conductor. (B) Mechanism of the absorption and reflection. The absorption in the high-emissivity state is from both the asymmetric Fabry–Pérot (AFP) cavity and gap surface plasmon (GSP) resonance. The low emissivity state is caused by the intrinsic reflectance of the top metal and doped emeraldine salt (ES). (C) Metal-to-insulator (MIT) transition from the undoped emeraldine base (EB) to the doped, protonated ES form of PANI. A^- is the counterion. (D) Schematic diagram of the interfacial polymerization process in the solution. The aniline monomer in orange is oxidized and initiated at the interface for further chain growth. (E) Synthesis procedure of solution-processable PANI-CSA.

On the other hand, conducting polymers (CPs) feature the capability to modulate their optical properties continuously and reversibly through chemical reaction or electrochemical bias. The optical property changes are stable and can be easily manipulated across a wide range of temperatures. Polymers also offer tremendous degrees of freedom in terms of fabrication and molecular engineering to address the needs of diverse applications.[28−30] Considerable research efforts in polymer synthesis, side chain engineering, and postprocessing have been made to further expand the plasmonic and electrochromic performance by improving the charge carrier density and mobility.[28,31,32] In the longer-wavelength range, CPs have long been the popular candidates of mid-infrared (mid-IR) variable emissivity applications.[33−35] Compared to single-mode heating/cooling devices, CPs offer the possibility to actively tune the emissivity while maintaining it without any energy consumption.[36]

Meanwhile, metasurface design can enable more functionality and performance of CPs by enhancing the light−matter interaction and increasing the spectral tunability at a wide range of wavelengths that are not possible with conventional simple thin films. With rationally designed optical modes, the far-field electromagnetic wave characteristics can be fully controlled. With the tunable optical properties, multiple states of unconventional optical functionality can be achieved in one device.[15,37−43] For thermal and IR applications, Kirchhoff's law is employed to equate absorptivity and emissivity, providing directional emission control and increasing emissivity contrast to thermal emitters and radiative coolers.

The key challenge is to establish the synthesis−structure−property relationship that covers polymer chemistry/physics, the charge transport mechanism, and optical theories. Despite great effort to the development of materials, the long-wave IR optical properties of CPs are largely unexplored, especially when considering the properties at various states from various synthesis and processing conditions with complicated structure-dependent charge transport kinetics. In addition, the vast majority of CP-based IR electrochromic devices are limited to those lying in the insulating side of the Anderson−Mott transition, limiting the tuning mechanism to transmissive and lossy dielectric.[36]

In this work, we introduce solution-processable CP as the actively tunable material for applications in broadband variable thermoregulation metasurfaces. We synthesize tunable polyaniline (PANI) doped with camphor sulfonic acid (CSA), featuring its stability, high optical conductivity for intrinsic

https://doi.org/10.1021/acsphotonics.5c02077
ACS Photonics 2026, 13, 2338−2347

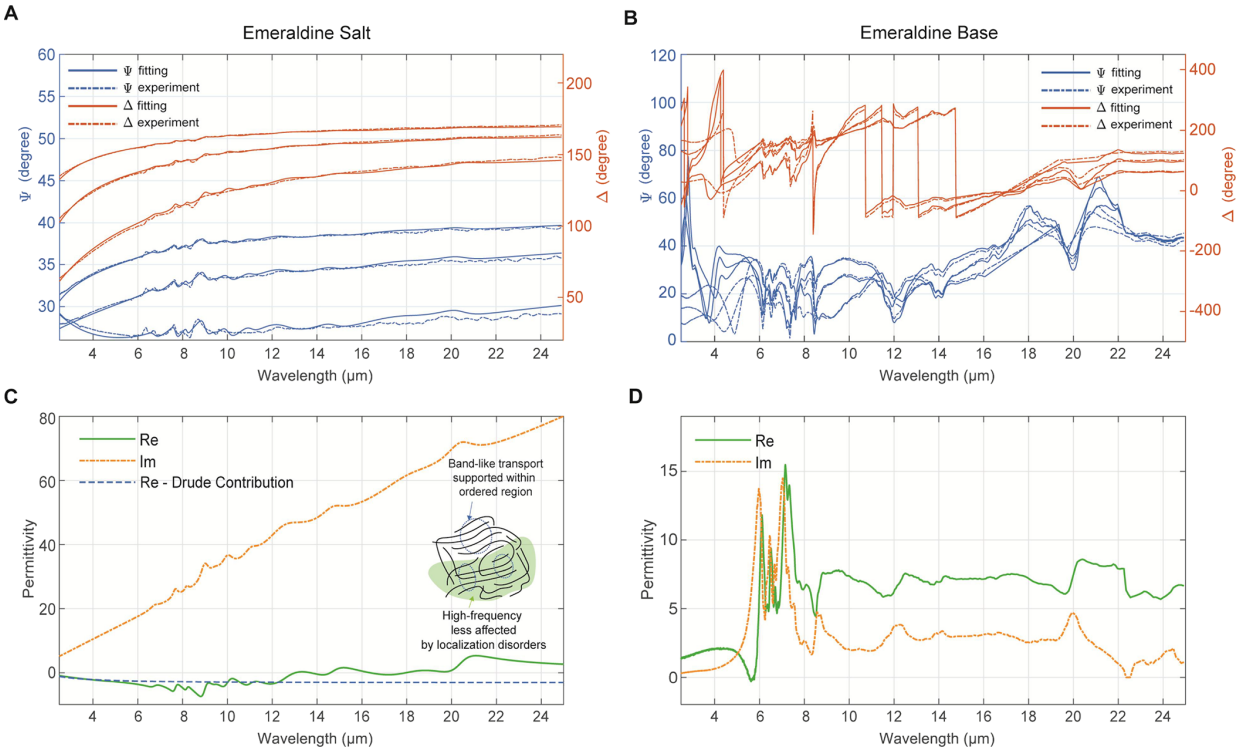

Figure 2. Optical properties of PANI-CSA from the spectroscopic ellipsometry measurement. (A, B) Spectroscopic ellipsometry data (Ψ, Δ) of fully doped ES (A) and moderately doped EB (B) on a Au substrate at angles of incidence of 55, 65, and 75°. (C, D) Complex permittivity dispersion of fully doped ES (C) and moderately doped EB (D). Dispersion contribution from the classical Drude model is plotted in a dashed curve. Note that the permittivity is always negative without the effects of chemical bonds and localization. The inset figure in (C) shows that the charge transport is affected by different extents of structural disorders when excited with different frequencies of light.

IR reflection, and scalable room-temperature polymerization process. The complex permittivities at its lossy dielectric and metallic states on the opposite side of the Anderson−Mott transition were characterized through IR spectroscopic ellipsometry. Finally, we performed design and optimization and demonstrated the potential of incorporating CPs for wide-angle dynamic metasurface emitter applications.

DEVICE DESIGN AND PRINCIPLE

We first consider the design principle of the metasurface perfect absorber. According to Kirchhoff's radiation law, for a reciprocal optical system at thermodynamic equilibrium, absorptivity should equal emissivity for the same wavelength, polarization, and angle. In other words, a broadband and wide-angle absorber with near-unity absorptivity will be an optimal thermal emitter. A perfect metasurface absorber is often accomplished by negating the reflectivity of an opaque surface, which involves the cancellation of backward-traveling electromagnetic wave responses from various interfaces or modes. One effective design is the metal−insulator−metal (MIM) structure, which features a dielectric spacer placed in between a metal cap and a metal substrate.[44] The variation of the spacer and/or the top cap with active materials is a common way to allow tunable functionality.[45] Tunable devices with resonant wavelength in mid-IR are able to control the heat loss of the object in daily life scenarios by their variable emissivity.

As shown in Figure 1A,B, the metasurface can be toggled between high and low emissivity by modulating the optical properties of the CP spacer. The spacer, PANI-CSA, is an active CP transitioning between lossy dielectric and reflective metal with varying doping level and oxidation state. PANI is known for the capability of undergoing Anderson−Mott transition from an insulator to a metal, exhibiting a wide range of DC conductivity from the order of 10 to up to 1100 S/cm.[46] The counteranion serves as an extrinsic dopant and changes the electronic structure of the CP (Figure 1C).

While it is possible for PANI-CSA to be metallic for the low-emissivity state, the synthesis is nontrivial. Metallic PANI-CSA emeraldine salt (ES) has only been demonstrated through low temperature self-stabilized dispersion polymerization at −35 °C.[46] This process also requires excellent nanostructure control during synthesis to achieve high molecular weight, high crystallinity, and an extremely low level of disorder to reach free-carrier, Drude-like charge transport.

Considering both the processability and the high reflectance required, we used room-temperature interfacial polymerization to synthesize PANI-CSA in m-cresol as the stock solution. As shown in Figure 1D, this method features the high molecular weight polymer chain acquired by confining the polymerization growth at the phase boundary between the solid oxidizer and liquid acidic monomer solution, suppressing numbers of polymerization initiation and the unfavorable side reaction.[47] Compared with most other synthesis methods, the resulting PANI-CSA has a much higher crystallinity. For example, we can observe from grazing-incident wide-angle X-ray scattering (GIWAXS) data showing that interfacial-polymerized PANI exhibits higher crystallinity and more prominent lamellar structures compared with electropolymerized PANI (Figures

https://doi.org/10.1021/acsphotonics.5c02077
ACS Photonics 2026, 13, 2338−2347

S1 and S2). Because of the high crystallinity and low degree of disorder, the ES state of interfacial polymerized PANI-CSA is intrinsically reflective, which is in stark contrast with CPs whose conducting form is dominated by absorption (high emissivity). This improvement of the optical conductivity is the key to significantly enhancing the reflectivity at the low-emissivity state, enabling a large emissivity dynamic range in conjunction with active metasurface design.

Figure 1E shows the steps of the synthesis. Aniline monomers were first polymerized with CSA and ground ammonium persulfate in chloroform at room temperature. The resulting mixture was washed with water and acetone to extract the PANI-CSA, followed by washing, dedoping, and redoping processes in m-cresol to accurately control the doping level. The final product was filtered to reduce the particle size due to aggregation before drop casting or spin coating. ES thin films were obtained by drop casting and drying at 60 °C on pristine Si or Au/Si wafer substrate, and the EB films were chemically dedoped with ammonium hydroxide surface treatment on the ES sample. All the samples used for electrical and optical measurements were prepared by interfacial polymerization. The detailed steps of synthesis and sample preparation are described in Experimental Procedure.

OPTICAL PROPERTIES OF PANI

We performed spectroscopic ellipsometry (Figure 2A,B) to understand the complex optical properties (Figure 2C,D) of ES and EB. The optical properties of fully doped ES and moderately doped EB are discussed in detail with Figure 2, as they are the two states that we utilize for optimal emissivity tuning the metasurface. The optical properties of fully dedoped EB are shown in Figure S3.

The mid-IR optical properties and reflectance of CPs are determined by their structure-dependent charge transport. The interfacial polymerized PANI-CSA studied here is affected by weak localization, and the optical conductivity at low frequency slightly decreases due to inhomogeneity. While the first-principles theoretical model to describe the optical properties of CPs in the metallic regime is yet to be developed, the localization-modified Drude (LMD) model has been extensively used to describe the correlation between optical conductivity and structural disorders from the phenomenological and physical perspectives. A first-order correction considering the weak localization and inelastic diffusion in optical conductivity is used to feature the strength of disorder.[48] The LMD optical conductivity from the standard Drude model is defined as

$$\sigma_{\mathrm{LMD}}(\omega) = \sigma_{\mathrm{Drude}}(\omega)\left[1 - \frac{C}{(k_{\mathrm{F}}l)^2}(1 - \sqrt{3\omega\tau})\right]$$

where $\sigma_{\mathrm{Drude}}(\omega)$ is the frequency-dependent optical conductivity from classical Drude model, the fitting term $\frac{C}{(k_{\mathrm{F}}l)^2}$ is treated as a single localization parameter with C being unity, k_{F} is the Fermi wavevector, l is the carrier mean free path, and τ is the scattering time. Note that the localization parameter theoretically determines the decrease of DC conductivity from $\sigma_{\mathrm{Drude}}(0)$ to $\sigma_{\mathrm{LMD}}(0) = \sigma_{\mathrm{Drude}}(0)\left[1 - \frac{C}{(k_{\mathrm{F}}l)^2}\right]$ due to the localization. Here, when $\frac{C}{(k_{\mathrm{F}}l)^2}$ was 0.18 in the model, the $\sigma_{\mathrm{LMD}}(0)$ = 465 S/cm is in excellent agreement with the 445 S/cm DC conductivity measured in the experiment (Figure S4). Since the localization is weak, we also note that it is possible to fit the model with classical Drude and Lorentz oscillators with relatively small errors when predicting DC and low-frequency optical conductivity.

The complex permittivity of ES from Drude−Lorentz model fitting in Figure 2A is shown in Figure 2C. The zero-crossing of real permittivity from negative to positive at 14 μm is characteristic of a weak localization system. This is theoretically predicted by the localization-modified Drude model with Kramers−Kronig transformation and experimentally observed in weakly localized CPs (Text S1). For samples with stronger localization, the optical conductivity will significantly decrease (Figure S5).

In addition to the great optical conductivity of the metallic conducting state, the ability to span across both sides of the MIT is also one of the key criteria in choosing the active material used in the metasurface. As opposed to the PANI system, it can be more challenging to practically switch some of the metallic CPs across the MIT. An example is shown in Figure S6. When the sulfuric acid-treated PEDOT:PSS (poly(3,4-ethylenedioxythiophene)polystyrenesulfonate) is dedoped in 1 M ammonia solution or 0.5 M $NaBH_4$/1 M NaOH, its DC conductivity decreases from 3150 to 426 and 432 S/cm, respectively, but all of these states are metallic and reflective in the mid-IR wavelength regime, indicating inadequate tunability compared to PANI.

With the ability to switch to the insulating side, moderately doped EB exhibits lossy dielectric characteristics with significantly lower DC conductivity, lying on the insulating side of the MIT transition. This behavior arises from a combination of disorder-induced localization and a reduction in charge carrier concentration in response to a doping level change. The mid-IR optical properties of PANI-EB feature the strong absorption from infrared active vibrational (IRAV) modes caused by bound polarons.[49,50] As an absorption caused by correlated interaction between charge carriers and structural distortion, IRAV peaks in CPs are known to be present and dependent on the ability of delocalization associated with different backbones, side chain species, and doping levels.[28,51]

In PANI-EB, the strongest IRAV absorption peaks are at the wavelength between 5 and 10 μm. These peaks are assigned to ring stretching, protonated imine and amine, C−H/C−N bond vibrations, and structural disorders[49] (Table S1 and Figure S7). Complex permittivity of EB in Figure 2D is derived from point-by-point fitting of the ellipsometer data (compared to the Kramer−Kronig consistent model in Figure 2B), to account for small features caused by both polarons and disorders. The comparison between the permittivity derived from the KK-consistent model and the point-by-point fitting is in Figure S8.

Insulating EB with a lower doping level shows much stronger IRAV absorption than ES, whose optical response is dominated by the negative real permittivity due to high Fermi velocity and conductivity.[46] The appearance of IRAV peaks is similarly observed in VO_2 transition and PANI-CSA ES with even higher DC conductivity, although the trend may vary or even become opposite, as in the case of polythiophenes and polyacetylenes where the dopant-induced vibration has a much higher mobility.[25,28,46,52]

Between 10 and 25 μm, moderately doped EB behaves like a less dispersive, lossy dielectric. Its imaginary permittivity is larger compared to fully dedoped EB, indicating this

https://doi.org/10.1021/acsphotonics.5c02077
ACS Photonics 2026, 13, 2338−2347

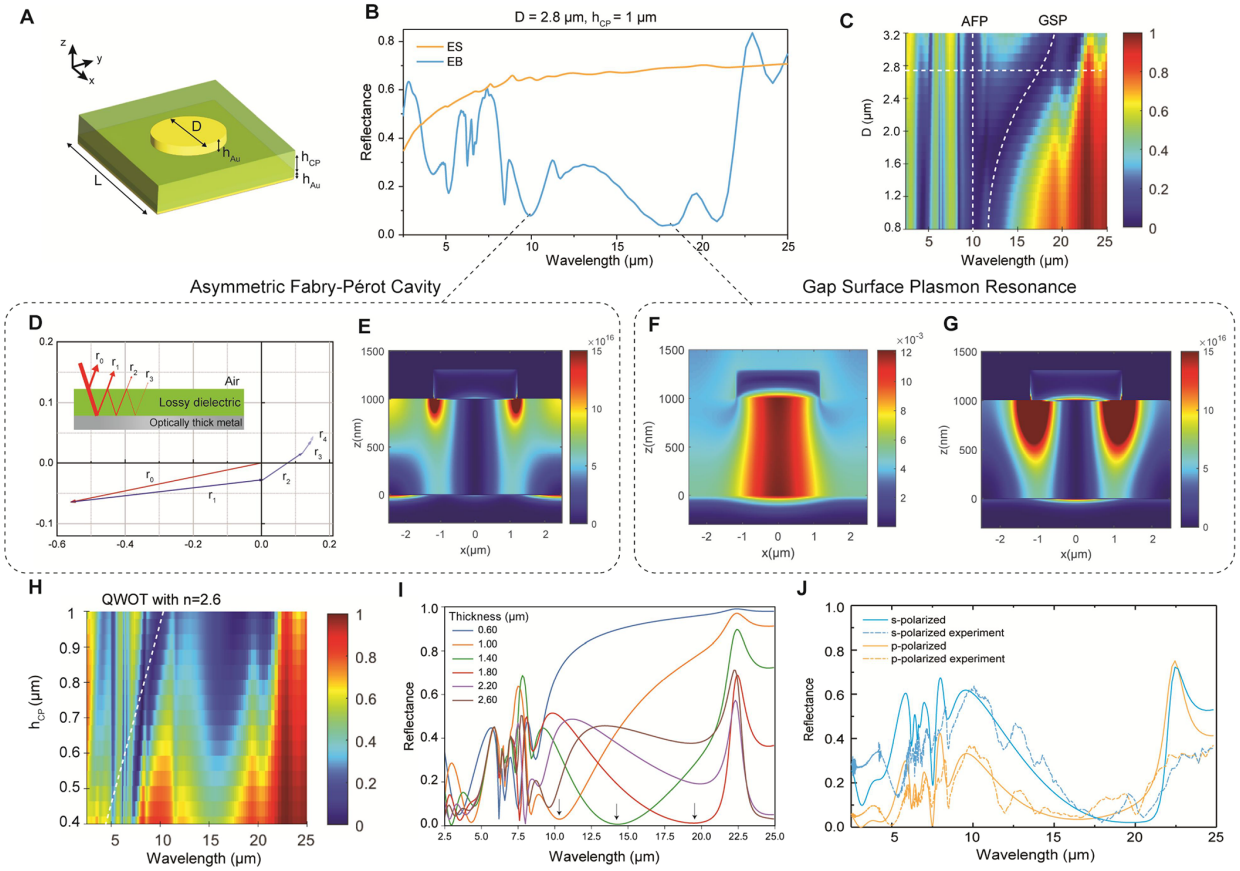

Figure 3. Quantitative analysis of the tunable metasurface thermal emitter based on the PANI-CSA. (A) Schematic diagram of the meta-atom within a unit cell. (h_{Au} = 150 nm, L = 5 μm) is fixed for all simulations in Figure 3. (B) Calculated reflection spectra of the Au/CP/Au metasurface absorber with CP being PANI in the ES and EB states. Optical properties measured from spectroscopic ellipsometry in Figure 2 were used. (C) Reflection spectral map with respect to the disk diameter (h_{Au} = 150 nm, h_{CP} = 1 μm). The two dashed white lines correspond to the absorption of AFP and GSP at each thickness. (D) Phasor representation of the first five orders of reflection from r_0 to r_4. Inset: working principle of AFP cavity due to multiple reflections at interfaces. (E) Optical power loss distribution ($-0.5\omega|E|^2\varepsilon''$) across the center of meta-atom (y = 0, D = 2.4 μm) at λ = 10 μm mainly from the contribution of AFP. (F, G) Simulated amplitude of the y-component of magnetic field distribution (F) and optical power loss profile (G) across the center of the meta-atom (y = 0, D = 2.4 μm) corresponding to the GSP absorption. (H) Reflection spectra with respect to the thickness of CP (D = 2.4 μm). The dashed white line indicates the corresponding AFP absorption at quarter wave optical thickness with n = 2.6 (I) Calculated reflection spectra of AFP resonance (labeled with black arrows) with EB at various thicknesses. (J) Reflection spectra at s- and p-polarizations with 50° angle of incidence from experiments and calculations. All simulations here were performed under normal incidence, except for that in Figure 3J.

transitional state involving a mixture of metallic and insulating phase. The small absorption features are also related to the delocalization of the doped polymer chain. This intermediate state parallels the coexistence of metallic and insulating domains observed in phase-changing materials during the metal-insulatior transition. These similarities underscore the duality of the optical property changes in PANI and VO_2, where both materials exhibit strong vibrational absorption in the insulating phase and a shift toward high absorption before the intrinsic reflectivity in the metallic phase as the conductivity becomes higher. The metal-insulatior transition in PANI-CSA highlights the dynamic nature of the optical responses and their potential for actively tunable applications.

DYNAMICALLY TUNABLE PANI IN THE METASURFACE

Using experimentally measured optical properties, we demonstrate the concept of dynamic metasurface emitter through finite-difference time-domain (FDTD) simulation in both ES and EB states of PANI. The structure of the meta-atom is shown in Figure 3A. A continuous PANI spacer is placed in between an Au nanodisk and a back reflector substrate, resulting in a MIM perfect absorber configuration. With fixed metal thickness (t_{Au}) and unit cell size (L), the reflectance spectra of the metasurface are dependent on the thickness of the CP spacer (h_{CP}), diameter of the metal disk (D), and optical properties of CP. A thickness of 150 nm is fixed for metal to ensure it can support the magnetic dipole, and L is 5 μm to prevent an undesirable near-field effect and optimize the contrast.[53]

For the high-emissivity states of the metasurface, we utilize the high index and lossy properties of EB to introduce two absorption mechanisms: an asymmetric Fabry–Pérot (AFP) cavity and gap surface plasmon (GSP) resonance, in the long-wavelength region. In Figure 3B, the reflectance spectra at both emissivity states are plotted with periodic meta-atoms with

https://doi.org/10.1021/acsphotonics.5c02077
ACS Photonics 2026, 13, 2338−2347

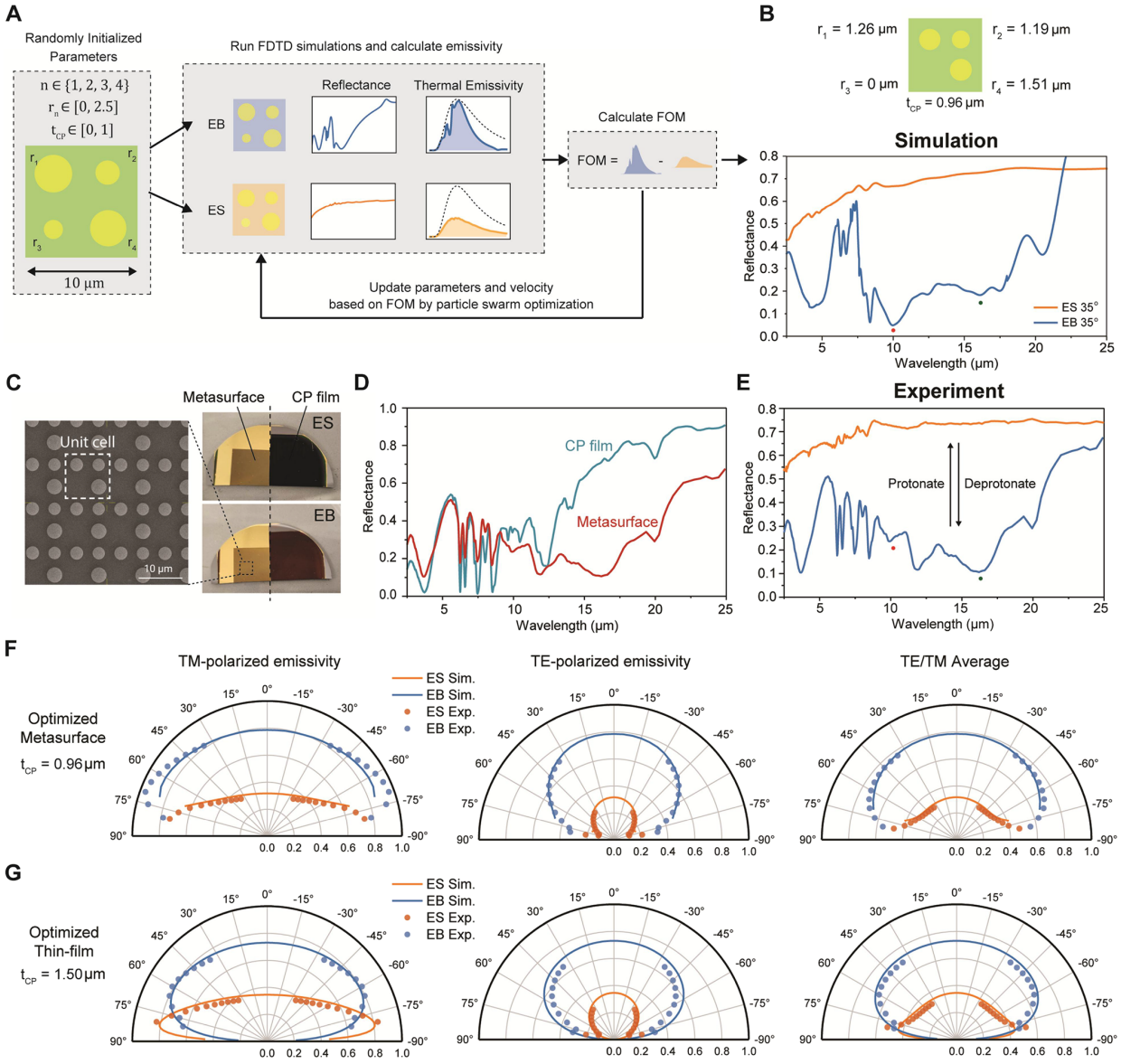

Figure 4. Forward design and experimental demonstration of tunable metasurface for broadband thermal emission by multiple meta-atoms. (A) Design process by FDTD simulation and particle swarm optimization. (B) Top view of the metasurface design and the corresponding simulated IR reflection spectra at a 35° incidence angle, averaged over TM and TE polarizations. The red and green dots indicate the AFP and GSP, respectively. (C) SEM image (left panel) and photographs (right panel) of the fabricated sample, which contains two regions: one with a metal-disk metasurface and one with only the CP thin film. Both regions are shown before and after five cycles of redoping (ES) and dedoping (EB). (D) Measured reflectance spectra of the metasurface and CP-film regions in the EB state at a 35° incidence angle after five cycles of dedoping and redoping, averaged over TM and TE polarizations. The difference highlights GSP absorption at long wavelength exclusively in the metasurface configuration. (E) Measured reflectance spectra of the metasurface after five cycles of dedoping and redoping at a 35° angle of incidence, averaged over TM and TE polarizations. The red and green dots indicate the AFP and GSP absorption, respectively. (F, G) Emissivity with TE polarization (left panels), TM polarization (middle panels), and their average (right panels) at 34 °C (307.15 K) of optimized metasurface with h_{CP} = 0.96 μm (F) and optimized thin-film CP with h_{CP} = 1.50 μm (G). The solid lines are simulations, and the circles are experimental data.

parameter (h_{CP}, D) = (1, 2.8) μm. The results demonstrate a prominent broadband reflectance contrast of two emissivity states between 8 and 22 μm from the combined effect of chemical absorption, AFP, and GSP resonance. The absorption peaks at 10 and 18 μm correspond to AFP and GSP, respectively. In Figure 3C, we recorded the simulated reflectance spectra with respect to disk diameter (D) and the absorption peak position of both resonances, which clearly depicts the independence and the dependence of AFP and GSP on disk diameter, respectively. This dependency is also experimentally demonstrated in Figure S9, which measures the reflectance spectra of the metasurface with different disk sizes.

As shown in the phasor diagram in Figure 3D, the AFP cavity here refers to the structure of a lossy dielectric with a quarter wave optical thickness (QWOT) on top of a reflective metallic substrate. The summation of multiple reflections

https://doi.org/10.1021/acsphotonics.5c02077
ACS Photonics 2026, 13, 2338−2347

cancels out the first reflection r_0 due to the absorption and optical path difference when propagating.[26,54] As a result, AFP resonance is dependent only on h_{CP} and material properties. When the dielectric layer is sufficiently lossy, the AFP resonance allows wide angles of incidence at different polarization. The inset in Figure 3D shows the phasors of multiple reflection coefficients up to r_4 with 1 μm-thick EB (n = 2.6 + 0.42i) on a metal substrate (n = 7.77 + 19.04i) at normal incidence at 10.25 μm. Figure 3E shows that the optical power loss ($-0.5\omega|E|^2\varepsilon''$) primarily locates near the top interface with substantial contribution from the metal ohmic loss.

As for the GSP, its magnetic field distribution (Figure 3F) at the resonance wavelength shows the prototypical magnetic dipole generated by the strong field confinement between the Au nanodisk and the back reflector. Figure 3G depicts the optical power loss, highlighting the distribution of energy dissipation, which is predominantly governed by the CP spacer due to the lossy nature of insulating EB. This emphasizes the critical role of the CP spacer in modulating the optical response of the metasurface, where its lossy dielectric properties enhance light absorption through mechanisms such as the AFP cavity and GSP resonance. It is worth noting that GSP resonance can also be observed in the isolated CP spacer, where AFP absorption is absent (Figure S10).

Since the 5−10 μm-wavelength range is dominated by IRAV absorptions, the film thickness should be larger than 1 μm to fully utilize AFP at the longer wavelength to minimize overlap and unnecessary coupling. As shown in Figure 3H, we plot the thickness-dependent reflection spectra and labeled the QWOT when n = 2.6 and h_{CP} from 0.4 to 1 μm to visualize the overlap of AFP and IRAV peaks. To show the tunability of AFP at resonant wavelengths above 10 μm, Figure 3I shows the calculated reflectance spectra of the thicker CP spacer in the EB state. In Figure 3J, AFP is further validated by experimentally measuring the specular IR reflectance of the EB thin film at a 50° angle of incidence for two different polarizations and compared with theoretical calculation by multilayer Fresnel equations.

FORWARD DESIGN AND PERFORMANCE OF THE METASURFACE

The intrinsic tunability of CP's optical property and the metasurface geometry parameter space contain vast degrees of freedom, enabling us to design an active thermoregulator with improved performance and functionality. As shown in Figure 4A, we designed and optimized the performance of the structure parameters by hybridizing meta-atoms, including the disk radii (r_1 to r_4) and the thickness of CP spacer (t_{CP}), which determine the AFP and GSP resonance absorption in the high-emissivity state. The unit cell size of metasurface and the height of the Au disks were fixed at 10 μm and 150 nm, respectively. We then ran the FDTD simulations to calculate the figure of merit (FOM) of the tunable metasurface emitter. The FOM is defined as the difference of the weighted-average emissivity at two emissivity states of the metasurface under normal incidence with respect to blackbody at 34 °C between 2.5 and 25 μm:

$$\mathrm{FOM} = \frac{\int_{2.5}^{25} [\varepsilon_{EB}(\lambda, r, t_{CP}) - \varepsilon_{ES}(\lambda, r, t_{CP})] I(\lambda) \mathrm{d}\lambda}{\int_{2.5}^{25} I(\lambda) \mathrm{d}\lambda}$$

where ε_{EB} and ε_{ES} correspond to the metasurface emissivity at the EB and ES states, respectively, and $I(\lambda) = \frac{2hc^2}{\lambda^5} \frac{1}{e^{hc/\lambda k_B T} - 1}$, in which h is the Planck constant, c is the speed of light, k_B is the Boltzmann constant, and T is 34 °C (307.15 K). The forward design and optimization shown in Figure 4A was performed through particle swarm optimization with 20 particles initialized for 20 epochs of parameter update. The result of optimized reflection spectra and device structure is illustrated in Figure 4B. It is noteworthy that the optimization process can minimize or eliminate one of the four disks, resulting in only AFP in that unit, which is possibly due to the strong weighting factor near 10 μm that favors AFP over GSP. It also follows the pattern to utilize disks with similar diameters within the GSP absorption bandwidth. We opted for the structure where one of the disks is minimized, resulting in only AFP in that unit. The final optimized parameter used in our experiment is (r_1, r_2, r_3, r_4, t_{CP}) = (1.26, 1.19, 0, 1.51, and 0.96) μm.

We then fabricated the numerically optimized active metasurface thermal emitter by photolithographically patterned Au microdisks on a spin-coated EB thin film with the proper doping level on the Au substrate. The detailed process of fabrication can be found in the Experimental Procedure section. The scanning electron microscopy (SEM) image in Figure 4C confirms the dimensions and the fabrication robustness. Also, in Figure 4C, the right panel shows the pictures of the samples, with the micropatterned metasurfaces on the left and the plain thin film on the right as the baseline references to monitor potential PANI property changes during the fabrication process. Figure 4D compares the measured reflectance spectra of the metasurface and thin-film regions. The result verifies the existence of chemical absorption peaks, AFP, and GSP resonance modes, and the stability of PANI when undergoing the fabrication process. In comparison, the reflectance spectra of plain thin-film PANI show much lower contrast at long wavelength because of the lack of GSP resonance.

The tunability of the metasurface thermal emitter was evaluated via chemical doping/dedoping. The reflectance spectrum at an angle of incidence at 35° was measured and is shown in Figure 4E with AFP and GSP absorption peaks labeled with red and green dots, respectively. The measured spectra are overall in good agreement with the simulated spectra in Figure 4B, although the experimental weighted-average emissivity contrast of 0.40 is slightly lower than 0.46 from the simulation. In the EB state, the AFP mode exists at 10 μm, slightly shorter than the simulation. The wavelength of GSP resonance is the same but with narrower resonance width. These discrepancies are mainly attributed to variations in optical properties introduced during the photolithography process involving multiple organic solvents, as well as to nonuniformity in the doping level. As a demonstration of the metasurface' switchability, we performed 100 cycles of switching and measured the reflectance spectra of both states at various cycles, showing the stability and reversibility of the emissivity modulation of the metasurface (Figure S13).

Similar to the great promise of "flat optics" brought by metasurfaces, our active metasurface thermal emitter also significantly reduces the required thickness. As shown in Figure 4F,G, the 0.96 μm-thick metasurface outperforms the plain thin film at each incident angle and polarization, resulting in 9.5% better hemispherical emissivity contrast despite the 1.5 times thickness difference of the active material. The

https://doi.org/10.1021/acsphotonics.5c02077
ACS Photonics 2026, 13, 2338−2347

simulation agrees well with the experimental measurement despite small variation of the sample thickness, showing the effectiveness and robustness of the co-design of the metasurface and polyaniline as an active optical material. In this study, the directional emissivities were calculated from reflectance spectra by Kirchhoff's law of thermal radiation, assuming the temperature of the sample is uniform. The material property change is also minimal with respect to temperature variation, as demonstrated by the reflectance spectra measured at different temperatures (Figure S14). Although this approach is sound and widely adopted, future direct emissivity measurements under actual thermal load and a controlled environment could be utilized to further optimize accuracy.

The result presented above is particularly important for active tunability. Although a high optical conductivity polymer with reasonably thin skin depth can achieve higher tunability by increasing the thickness (i.e., increasing the emissivity at the dedoped state while maintaining low emissivity at the doped state), excessive thickness will strongly inhibit the chemical species diffusion and reaction kinetics, creating a fundamental bottleneck for high-speed modulation. Larger thickness can also negatively impact the devices' durability due to the volume change and the mechanical stress built up at the interface, which can cause thin-film delamination.

CONCLUSIONS

In summary, we synthesized solution-processable PANI-CSA with high optical conductivity in the mid-IR and used reversible chemical tuning to vary its doping level, ultimately enabling a high-performance active metasurface thermal emitter. Through IR spectroscopic ellipsometry, we demonstrated the transition of PANI-CSA from a reflective metal with weak charge localization to a lossy dielectric neutral state. Combined with nanophotonics structure design that incorporates AFP and GSP modes at distinct wavelengths, the large refractive index modulation was used as an unconventional scheme to modulate the broadband thermal emissivity at the mid-to-long IR region. Finally, the optimization and evaluation procedure considering the weighted-average spectral directional emissivity can be directly performed with the optical properties measured from ellipsometry. We envision that the understanding of the PANI system and the co-design with metasurface theories will enable the development of highly efficient and multifunctional active optical materials based on the interdisciplinary research in correlated charge transport, organic chemistry, and (electro)chemical materials engineering, from nanomaterials design to device fabrication.

EXPERIMENTAL PROCEDURE

Synthesis of PANI-CSA and Thin-Film Preparation

The synthesis of PANI-CSA is based on the solid−liquid interfacial polymerization process.[47] The aniline monomer was distilled once prior to use in the polymerization reaction. Then, the interfacial polymerization reaction was conducted with a reaction mixture with a 1:2−2.5 aniline:CSA ratio, 4:1 aniline to ground ammonium persulfate (APS), at 25 °C; the reaction was carried for 24−48 h to ensure polymerization had concluded. The resulting reaction mixture was filtered twice via an aqueous funnel extraction. Then, the solvent was evaporated by using a rotary evaporator. Any residual water was manually removed from the solid, and then an acetone wash was conducted. The resulting powder was dried at 60 °C for 24 h under reduced pressure. The resulting emeraldine salt (ES) powder was dedoped using a 0.1 M NH_3 solution, stirred for 24 h. The resulting emeraldine base (EB) powder was washed thrice with water, acetone, and chloroform and then dried at 60 °C for 24 h under reduced pressure. Finally, ES was reformed by mixing the EB and CSA(+) powder in a 1:0.5 molar ratio with a mortar and pestle.

Thin films were formed by mixing the appropriate amount of ES in m-cresol to form a 1.5 wt % solution for samples with different thicknesses. This was stirred at 50 °C for 24−48 h in a silicone-oil bath for even heating. While warm, the solution was filtered with 2.7 μm syringe filters. This solution was drop-casted onto Au-coated silicon wafers, which were sonicated, washed, and preheated to 50 °C prior. Films were allowed to dry at 60 °C for 12−24 h.

Metasurface Fabrication

The fabrication of the metasurface is a lithography-defined metal lift-off process. A PANI-CSA layer was spin-coated or drop-casted on a Au substrate depending on the thickness requirement. An AZ nLOF 2020 negative photoresist was spin-coated at 4000 rpm for 45 s followed by soft baking at 110 °C for 1 min. The sample was then exposed to a 375 nm wavelength with an energy dose of 260 mJ/cm^2 and baked again at 110 °C for 1 min. The photoresist was developed in AZ 300MIF for 2 min. The metasurface pattern is formed by sequentially depositing 3 nm of Cr and 150 nm of Au by using electron-beam evaporation. Afterward, the sample was lifted off in acetone, rinsed with IPA and DI water, and finally blown dry with nitrogen. To achieve fully doped ES and moderately doped EB states, both metasurface and thin-film samples were reversibly doped and dedoped in 0.5 M sulfuric acid solution for 5 s and 0.2 M ammonium solution for 10 s, respectively.

Electrical Conductivity Measurement

Thickness is first measured from a KLA Tencor P-7 Surface Profilometer. Sheet resistance is measured from a Signatone Pro4 probe stand and a SP4 probe head along with Keysight B2901A. The conductivity is calculated as the reciprocal of the product of the thickness and sheet resistance.

IR Spectroscopic Ellipsometry

Infrared (IR) spectroscopic ellipsometry data were collected by an IR-VASE Mark II instrument from JA Woollam Co. and fitted with WVASE software. PANI-CSA ES and EB on Au/Si wafer samples were used for the measurement. IR ellipsometry spectra were collected at angles of incidence equal to 55, 65, and 75° from 2.5 to 25 μm. For the angle- and polarization-dependent emissivity measurement, we used Kirchoff's law and measured the IR reflectance spectra at angles of incidence that vary from 35 to 80°. A gold-plated Si wafer was used as a reference for the IR reflectance.

FTIR Spectrometry

Part of the emissivity spectra of samples were measured using an iS50 FTIR spectrometer (Thermo Fisher Scientific) with a diffuse gold integrating sphere. A gold-plated Si wafer was used as a reference for IR reflectance.

FDTD Simulation

All FDTD simulations were performed in commercial software Ansys Lumerical FDTD. The complex optical properties of PANI-CSA in the calculation were obtained by piecewise fitting experimentally measured spectroscopic ellipsometer data. The optical properties of Au are from the literature. The simulation region is a three-dimensional rectangular space with x and y directions being the unit cell size of the meta-atom (L), and 12 μm in the z direction. Periodic symmetric boundary conditions were applied on the x and y planes when the source is at normal incidence. The BFAST boundary condition is used when the incidence direction of the source is oblique. The broadband planewave source from 2.5 to 25 μm is placed at 10 μm above the substrate, and two field/power monitors with 500 frequency points and no apodization are at 0.5 μm above the source and 0.5 μm below the bottom of the substrate, respectively. An optical power absorption analysis group is placed on the cross section that goes through the center of the meta-atom. Twenty-five points were used for diameter sweeping, and 15 points were used for thickness sweeping.

https://doi.org/10.1021/acsphotonics.5c02077
ACS Photonics 2026, 13, 2338−2347

XRD and GIWAXS

XRD measurements were performed on a Rigaku SmartLab X-ray diffractometer with a HyPix-3000 detector and Cu Kα radiation. Diffraction patterns were recorded at a scan rate of 5° min^{-1}.

GIWAXS measurements were carried out at beamline 12-ID-B at the Advanced Photon Source, Argonne National Laboratory, at an X-ray energy of 13.3 keV, using a PerkinElmer XRpad 4343F detector. The incidence angle of the beam was 0.10°. The exposure time was 0.7 s.

■ ASSOCIATED CONTENT

Supporting Information

The Supporting Information is available free of charge at https://pubs.acs.org/doi/10.1021/acsphotonics.5c02077.

Structural analysis of PANI; optical properties and spectra of related conducting polymers; chemical fingerprint and assignment of PANI under FTIR analysis; calculations and experiments of reflectance spectra of thin-film and metasurfaces with different structures; reflectance spectra of metasurface at different temperatures; thermal camera images of metasurfaces (PDF)

Notes: Ting-Hsuan Chen, Qizhang Li, Xubing Wu, Kyle Hulle, Pei-Jan Hung, Qingsong Fan, Ching-Tai Fu, Po-Chun Hsu, Active Metasurface Thermal Emitters by Metallic Polymers, 2026, chemrxiv-2025-m586z, ChemRxiv, https://chemrxiv.org/doi/full/10.26434/chemrxiv-2025-m586z (accessed Mar. 25, 2026)

■ AUTHOR INFORMATION

Corresponding Author

Po-Chun Hsu − *Pritzker School of Molecular Engineering, The University of Chicago, Chicago, Illinois 60637, United States;* orcid.org/0000-0002-6509-9377; Email: pochunhsu@uchicago.edu

Authors

Ting-Hsuan Chen − *Pritzker School of Molecular Engineering, The University of Chicago, Chicago, Illinois 60637, United States; Thomas Lord Department of Mechanical Engineering and Materials Science, Duke University, Durham, North Carolina 27708, United States;* orcid.org/0000-0001-5664-8891

Qizhang Li − *Pritzker School of Molecular Engineering, The University of Chicago, Chicago, Illinois 60637, United States;* orcid.org/0000-0002-5454-4578

Xubing Wu − *Pritzker School of Molecular Engineering, The University of Chicago, Chicago, Illinois 60637, United States;* orcid.org/0009-0005-6425-3896

Kyle Hulle − *Department of Chemistry, The University of Chicago, Chicago, Illinois 60637, United States*

Pei-Jan Hung − *Pritzker School of Molecular Engineering, The University of Chicago, Chicago, Illinois 60637, United States;* orcid.org/0000-0003-2063-8522

Qingsong Fan − *Pritzker School of Molecular Engineering, The University of Chicago, Chicago, Illinois 60637, United States;* orcid.org/0000-0001-8555-769X

Ching-Tai Fu − *Pritzker School of Molecular Engineering, The University of Chicago, Chicago, Illinois 60637, United States*

Complete contact information is available at: https://pubs.acs.org/10.1021/acsphotonics.5c02077

Author Contributions

†T.-H.C., Q.L., and X.W. contributed equally to this work.

Author Contributions

P.-C.H. and T.-H.C. conceived the idea. T.-H.C. performed the calculations and the optical measurements. T.-H.C., Q.L., and Q.F. designed the metasurface structure and interpreted the data. T.-H.C., Q.L., X.W., and K.H. synthesized PANI and fabricated the metasurface samples. T.-H.C., X.W., P.-J.H. and C.-T.F. characterized the electrical and structural properties of PANI. T.-H.C and P-C.H wrote the manuscript with input from all coauthors.

Funding

This study was funded by the National Science Foundation (ECCS Award No. 2324286); Sony Corporation Research Award Program; and APS beam time award(s) (DOI: 10.46936/APS-188820/60013331) from the Advanced Photon Source, a U.S. Department of Energy (DOE) Office of Science user facility operated for the DOE Office of Science by Argonne National Laboratory under Contract No. DE-AC02-06CH11357.

Notes

The authors declare no competing financial interest.

■ ACKNOWLEDGMENTS

The authors acknowledge funding support and the Research Computing Center at The University of Chicago.

■ REFERENCES

(1) Karst, J.; et al. Electrically switchable metallic polymer nanoantennas. *Science* **2021**, *374*, 612−616.
(2) Han, S.; et al. Complete Complex Amplitude Modulation with Electronically Tunable Graphene Plasmonic Metamolecules. *ACS Nano* **2020**, *14*, 1166−1175.
(3) Kaissner, R.; Li, J.; Lu, W.; Li, X.; Neubrech, F.; Wang, J.; Liu, N.; et al. Electrochemically controlled metasurfaces with high-contrast switching at visible frequencies. *Sci. Adv.* **2021**, *7*, No. eabd9450.
(4) Liu, X.; Padilla, W. J. Reconfigurable room temperature metamaterial infrared emitter. *Optica* **2017**, *4*, 430.
(5) Li, W.; Fan, S. Nanophotonic control of thermal radiation for energy applications [Invited]. *Opt Express* **2018**, *26*, 15995−16021.
(6) Baranov, D. G.; et al. Nanophotonic engineering of far-field thermal emitters. *Nat. Mater.* **2019**, *18*, 920−930.
(7) Fan, Z.; Hwang, T.; Lin, S.; Chen, Y.; Wong, Z. J. Directional thermal emission and display using pixelated non-imaging micro-optics. *Nat. Commun.* **2024**, *15*, 4544.
(8) Siegel, J.; et al. Electrostatic steering of thermal emission with active metasurface control of delocalized modes. *Nat. Commun.* **2024**, *15*, 3376.
(9) Lu, W.; Menezes, L. d. S.; Tittl, A.; Ren, H.; Maier, S. A. Active Huygens' metasurface based on in-situ grown conductive polymer. *Nanophotonics* **2024**, *13*, 39−49.
(10) Xu, T.; et al. High-contrast and fast electrochromic switching enabled by plasmonics. *Nat. Commun.* **2016**, *7*, 10479.
(11) Li, Q.; Chen, T.-H.; Hsu, P.-C. Use electrochemistry to charge the next dynamic thermal metamaterials. *Next Energy* **2024**, *3*, No. 100108.
(12) Doshi, S.; et al. Direct electron beam patterning of electro-optically active PEDOT:PSS. *Nanophotonics* **2024**, *13*, 2271−2280.
(13) Karst, J.; et al. *Electro-active metaobjective from metalenses-on-demand. Nat. Commun.* **2022**, *13*, 7183.
(14) Qazilbash, M. M.; et al. Mott transition in VO2 revealed by infrared spectroscopy and nano-imaging. *Science* **2007**, *318*, 1750−1753.

(15) Wang, Y.; et al. Electrical tuning of phase-change antennas and metasurfaces. *Nat. Nanotechnol* **2021**, *16*, 667−672.
(16) Wang, Y.; et al. Sustainable, low-cost, high-contrast electrochromic displays via host-guest interactions. *Proc. Natl. Acad. Sci. U. S. A.* **2024**, *121*, No. e2401060121.
(17) Wang, Z.; et al. Viologen-Immobilized 2D Polymer Film Enabling Highly Efficient Electrochromic Device for Solar-Powered Smart Window. *Adv. Mater.* **2022**, *34*, No. e2106073.
(18) Chen, S.; et al. On the anomalous optical conductivity dispersion of electrically conducting polymers: ultra-wide spectral range ellipsometry combined with a Drude−Lorentz model. *Journal of Materials Chemistry C* **2019**, *7*, 4350−4362.
(19) Chen, S.; et al. Conductive polymer nanoantennas for dynamic organic plasmonics. *Nat. Nanotechnol* **2020**, *15*, 35−40.
(20) Song, I.; et al. An n-doped capacitive transparent conductor for all-polymer electrochromic displays. *Nature Electronics* **2024**, *7*, 1158−1169.
(21) Balci, O.; Polat, E. O.; Kakenov, N.; Kocabas, C. Graphene-enabled electrically switchable radar-absorbing surfaces. *Nat. Commun.* **2015**, *6*, 6628.
(22) Ergoktas, M. S.; et al. Multispectral Graphene-Based Electro-Optical Surfaces with Reversible Tunability from Visible to Microwave Wavelengths. *Nat. Photonics* **2021**, *15*, 493−498.
(23) Chakraborty, R. D.; Postiglione, W. M.; Ghosh, S.; Mkhoyan, K. A.; Leighton, C.; Ferry, V. E.; et al. Optical Properties of Electrochemically Gated La1−xSrxCoO3−δ as a Topotactic Phase-Change Material. *Adv. Opt. Mater.* **2023**, *11*, 2300098.
(24) Niklasson, G. A.; Berggren, L.; Larsson, A.-L. Electrochromic tungsten oxide: the role of defects. *Sol. Energy Mater. Sol. Cells* **2004**, *84*, 315−328.
(25) Wan, C.; Zhang, Z.; Woolf, D.; Hessel, C. M.; Rensberg, J.; Hensley, J. M.; Xiao, Y.; Shahsafi, A.; Salman, J.; Richter, S.; Sun, Y.; Qazilbash, M. M.; Schmidt-Grund, R.; Ronning, C.; Ramanathan, S.; Kats, M. A.; et al. On the Optical Properties of Thin-Film Vanadium Dioxide from the Visible to the Far Infrared. *Ann. Phys.* **2019**, *531*, 1900188.
(26) Kats, M. A.; Sharma, D.; Lin, J.; Genevet, P.; Blanchard, R.; Yang, Z.; Qazilbash, M. M.; Basov, D. N.; Ramanathan, S.; Capasso, F.; et al. Ultra-thin perfect absorber employing a tunable phase change material. *Appl. Phys. Lett.* **2012**, *101*, 221101.
(27) King, J.; et al. Electrically tunable VO2−metal metasurface for mid-infrared switching, limiting and nonlinear isolation. *Nat. Photonics* **2024**, *18*, 74−80.
(28) Shen, D. E.; Goins, C. L.; Jones, A. L.; Österholm, A. M.; Reynolds, J. R. Design Rules for High Contrast Mid-Infrared Electrochromism in Conjugated Polymers. *ACS Materials Letters* **2024**, *6*, 528−534.
(29) Savagian, L. R.; Österholm, A. M.; Shen, D. E.; Christiansen, D. T.; Kuepfert, M.; Reynolds, J. R.; et al. Conjugated Polymer Blends for High Contrast Black-to-Transmissive Electrochromism. *Adv. Opt. Mater.* **2018**, *6*, 1800594.
(30) Miao, H.; et al. Viologen-based solution-processable ionic porous polymers for electrochromic applications. *Chem. Sci.* **2024**, *15*, 7576−7585.
(31) Ponder, J. F., Jr.; et al. Significant Enhancement of the Electrical Conductivity of Conjugated Polymers by Post-Processing Side Chain Removal. *J. Am. Chem. Soc.* **2022**, *144*, 1351−1360.
(32) Yang, Y.; Liu, Z.; Zhang, G.; Zhang, X.; Zhang, D. The Effects of Side Chains on the Charge Mobilities and Functionalities of Semiconducting Conjugated Polymers beyond Solubilities. *Adv. Mater.* **2019**, *31*, No. e1903104.
(33) Brooke, R.; et al. Infrared electrochromic conducting polymer devices. *Journal of Materials Chemistry C* **2017**, *5*, 5824−5830.
(34) Kuang, C.; Chen, S.; Liao, M.; Rahmanudin, A.; Banerjee, D.; Edberg, J.; Tybrandt, K.; Zhao, D.; Jonsson, M. P.; et al. Electrically tunable infrared optics enabled by flexible ion-permeable conducting polymer-cellulose paper. *npj Flexible Electron.* **2024**, *8*, 55.
(35) Gong, H.; et al. Recent progress and advances in electrochromic devices exhibiting infrared modulation. *Journal of Materials Chemistry A* **2022**, *10*, 6269−6290.
(36) Chen, T. H.; et al. A kirigami-enabled electrochromic wearable variable-emittance device for energy-efficient adaptive personal thermoregulation. *PNAS Nexus* **2023**, *2*, No. pgad165.
(37) Li, Q.; et al. Metasurface optofluidics for dynamic control of light fields. *Nat. Nanotechnol* **2022**, *17*, 1097−1103.
(38) de Jong, D.; et al. Electrically switchable metallic polymer metasurface device with gel polymer electrolyte. *Nanophotonics* **2023**, *12*, 1397−1404.
(39) Lee, Y.; Karst, J.; Ubl, M.; Hentschel, M.; Giessen, H. Dynamic beam control based on electrically switchable nanogratings from conducting polymers. *Nanophotonics* **2023**, *12*, 2865−2871.
(40) Kaissner, R.; Renz, B.; Neubrech, F.; Hu, Y.; Liu, N. An Electrochemically Programmable Metasurface with Independently Controlled Metasurface Pixels at Optical Frequencies. *Nano Lett.* **2024**, *24*, 9961−9966.
(41) Yu, P.; Li, J.; Liu, N. Electrically Tunable Optical Metasurfaces for Dynamic Polarization Conversion. *Nano Lett.* **2021**, *21*, 6690−6695.
(42) Kazi, S.; et al. n-Type redox-tuneable conducting polymer optical nanoantennas. *J. Mater. Chem. C Mater.* **2024**, *12*, 17469−17474.
(43) Xiong, K.; et al. Video-Rate Switching of High-Reflectivity Hybrid Cavities Spanning All Primary Colors. *Adv. Mater.* **2023**, *35*, No. e2302028.
(44) Watts, C. M.; Liu, X.; Padilla, W. J. Metamaterial electromagnetic wave absorbers. *Adv. Mater.* **2012**, *24*, OP98−120−OP181.
(45) Tang, K.; et al. Temperature-adaptive radiative coating for all-season household thermal regulation. *Science* **2021**, *374*, 1504−1509.
(46) Lee, K.; et al. Metallic transport in polyaniline. *Nature* **2006**, *441*, 65−68.
(47) Kim, C.; Oh, W.; Park, J.-W. Solid/liquid interfacial synthesis of high conductivity polyaniline. *RSC Adv.* **2016**, *6*, 82721−82725.
(48) Mott, N. F.; Kaveh, M. Metal-insulator transitions in non-crystalline systems. *Adv. Phys.* **1985**, *34*, 329−401.
(49) McCall, R. P.; et al. Massive polarons in large-energy-gap polymers. *Phys. Rev. B Condens Matter* **1989**, *39*, 10174−10178.
(50) Yang, C.-C.; et al. Platinum Particles Embedded into Nanowires of Polyaniline Doped With Poly(Acrylic Acid-co-Maleic Acid) as Electrocatalyst for Methanol Oxidation. *Int. J. Electrochem. Sci.* **2011**, *6*, 1642−1654.
(51) Jacobs, I. E.; et al. Structural and Dynamic Disorder, Not Ionic Trapping, Controls Charge Transport in Highly Doped Conducting Polymers. *J. Am. Chem. Soc.* **2022**, *144*, 3005−3019.
(52) Lee, K.; Menon, R.; Yoon, C. O.; Heeger, A. J. Reflectance of conducting polypyrrole: Observation of the metal-insulator transition driven by disorder. *Phys. Rev. B Condens Matter* **1995**, *52*, 4779−4787.
(53) Hao, J.; et al. High performance optical absorber based on a plasmonic metamaterial. *Appl. Phys. Lett.* **2010**, *96*, 251104.
(54) Kats, M. A.; Capasso, F. Optical absorbers based on strong interference in ultra-thin films. *Laser & Photonics Reviews* **2016**, *10*, 735−749.

https://doi.org/10.1021/acsphotonics.5c02077
ACS Photonics 2026, 13, 2338−2347